

How Much Capacity Does EEG Denoising Need? Ultra-Compact Networks reveal Benchmark Saturation and Metric-Utility Gap

Jasmeet Singh Bindra^{1,*}, Siddharth Panwar² and Shubhajit Roy Chowdhury²

¹Indian Knowledge Systems and Mental Health Applications (IKSMHA) Center, Indian Institute of Technology Mandi, Himachal Pradesh, India

²School of Computing and Electrical Engineering, Indian Institute of Technology Mandi, Himachal Pradesh, India

*Author to whom any correspondence should be addressed.

E-mail: D24059@students.iitmandi.ac.in; siddharth.panwar@iitmandi.ac.in; src@iitmandi.ac.in

Keywords: EEG denoising, model complexity, parameter efficiency, brain-computer interface, benchmark analysis, lightweight neural networks

Abstract

Objective. Deep Learning based EEG denoising architectures have scaled from tens of thousands to tens of millions of parameters, yet to our knowledge, no prior study has isolated model capacity as the experimental variable or tested whether the reconstruction metrics these models optimize predict downstream neural-signal utility. We address both gaps. **Approach.** We kept architecture, loss, data split, and training recipe fixed and swept only channel width from 1.05K to 40.26K trainable parameters in a minimal depthwise-separable convolutional U-Net. Models were evaluated on the EEGDenoiseNet benchmark, a million-segment mixed-artifact corpus, two cross-dataset BCI zero-shot transfer tests, controlled retraining of established baselines under the same pipeline, and downstream motor-imagery classification with five decoder families across all nine BCI Competition IV-2a subjects. **Main Results.** Reconstruction performance saturated by 3-6.5K parameters across all benchmark settings, with post-elbow gains of at most 0.015 correlation coefficient (CC) per \log_{10} -parameter unit. An 8.46M-parameter EEGDN CNN retrained under the same pipeline matched the 40.26K parameter compact variant on EOG, a $200\times$ parameter gap yielding no reconstruction advantage, while a second-family Patch-Transformer control reproduced the same diminishing-return shape. Downstream evaluation exposed a classifier-dependent metric-utility gap: reconstruction-optimized denoising significantly degraded CSP+LDA motor-imagery classification across all nine subjects and three artifact types (best denoised accuracy 0.547 versus 0.612 noisy baseline; Bonferroni $p = 0.0488$), with the gap persisting on naturally recorded trials ($\Delta = -0.047$; BH-FDR $q = 0.0049$). End-to-end neural decoders showed variable or neutral effects, indicating that the gap is classifier-dependent. **Significance.** Standard EEG denoising benchmarks are saturated far below the capacity of current models, and the reconstruction metrics they reward do not predict downstream BCI utility. Ultra-compact models at 33-46 KB and 1.27-2.61M FLOPs per segment are practical for edge EEG deployment. These findings argue for capacity-controlled evaluation, harder benchmarks with task-aware endpoints, and mandatory downstream validation in future denoising studies.

1 Introduction

EEG denoising architectures have grown from benchmark CNN/RNN baselines to U-Nets, adversarial hybrids, Transformers, and state-space models, with parameter counts spanning tens of thousands to tens of millions [1, 2, 3, 4, 5]. This growth has improved reconstruction metrics on semi-synthetic benchmarks, but two basic questions remain unresolved: how much capacity do these benchmarks actually require, and do reconstruction metrics predict downstream EEG utility?

EEG is central to brain-computer interfaces (BCIs), clinical neuroscience, cognitive monitoring, and neurotechnology because it is non-invasive, portable, and temporally precise. These same recordings are vulnerable to non-neural contamination from ocular, muscular, cardiac, line-noise, and electrode-related sources [6, 7]. Classical methods such as filtering, regression, ICA/BSS, artifact subspace reconstruction, and automated rejection remain valuable [8, 9, 10, 11, 12, 13, 14],

but heterogeneous artifacts and spectrally overlapping neural activity have motivated learned denoising models.

This raises two connected questions. First, how much model capacity does standard EEG denoising actually require? Existing comparisons typically evaluate one proposed architecture against a set of baselines, but they do not isolate capacity as the experimental variable. As a result, it is difficult to determine whether improved performance comes from a specific architectural mechanism, a larger parameter budget, training details, or benchmark saturation. Second, do reconstruction metrics measure the form of signal preservation that matters for downstream EEG use? Correlation coefficient (CC), root mean square error (RMSE), signal-to-distortion ratio (SDR), and related temporal or spectral errors quantify similarity to an assumed-clean reference. These metrics are essential for standardized benchmarking, but they do not directly test whether denoising preserves task-relevant neural features. This distinction is especially important because supervised EEG denoising benchmarks generally treat preprocessed EEG as the clean target. A model optimized to reproduce that target may achieve high reconstruction fidelity while still suppressing neural components that are useful for classification, detection, or interpretation.

We hold the architecture fixed and sweep only channel width from 1.05K to 40.26K parameters, evaluating reconstruction across EEGDenoiseNet, a large mixed-artifact corpus, BCI zero-shot transfer, controlled baseline retraining, compute profiling, and five downstream BCI decoder families. This design turns model capacity into the experimental variable rather than a hidden property of unrelated architectures.

Our contributions are threefold:

1. A controlled width sweep shows that reconstruction performance saturates by 3–6.5K parameters on the standard EEGDenoiseNet benchmark, a compositionally harder million-segment mixed-artifact corpus, and two cross-dataset BCI zero-shot transfer tests, with the pattern supported by a second-family Patch-Transformer control and same-pipeline EEGDN CNN and MicroWaveNet retraining.
2. Reconstruction-optimized denoising significantly degrades Common Spatial Patterns (CSP) + Linear-Discriminant Analysis (LDA) classification across all nine BCI IV-2a subjects and three artifact types ($p = 0.0098$, Bonferroni $p = 0.0488$ for synthetic EOG), with the gap persisting on real non-synthetic recordings, while end-to-end neural decoders show variable effects.
3. Base4–base6 models occupy 33–46 KB and require 1.27–2.61M FLOPs per segment, identifying deployment-ready operating points for embedded EEG systems.

Together, these results argue for capacity-controlled denoising evaluation, harder benchmarks, and task-aware validation that tests whether denoising preserves the neural information downstream applications require.

The capacity ceiling and metric–utility gap have direct implications for neural signal processing pipelines: practitioners risk degrading BCI performance by adopting reconstruction-optimized denoisers without downstream validation.

2 Related Work

2.1 Architectural Progression Without Capacity Control

Deep EEG denoising has progressed through increasingly specialized architectures, paralleling the broader growth of deep EEG analysis [15]. EEGDenoiseNet established a standard supervised setting in which a contaminated single-channel segment is mapped to an assumed-clean target and evaluated with reconstruction metrics [1]. Its CNN and RNN baselines (hereafter EEGDN CNN and EEGDN RNN) remain important reference points because they place early benchmark models at 8.40M and 787.0K parameters in our comparison, far above the ultra-compact regime.

Subsequent work introduced encoder-decoder, U-Net, generative, recurrent, Transformer, and state-space mechanisms. IC-U-Net and LRR-UNet extended U-Net-style recovery [2, 16]; AR-WGAN, DuoCL, and GCTNet introduced adversarial, recurrent, and hybrid CNN-Transformer components [3, 17, 18]; and Denoformer, CT-DCENet, and DenoiseMamba represent the high-capacity end of the progression [19, 4, 5]. Parameter counts at this end range from hundreds of thousands to tens of millions (e.g., EEGDN CNN 8.40M, CT-DCENet 38.10M), but most of these models lack publicly available code, making independent reproduction of their reported metrics difficult.

Lightweight models provide a counterpoint but still do not isolate capacity. DeepSeparator and MicroWaveNet occupy the 32–60K range and show that denoising does not always require

million-parameter models [20, 21]. LTDNet-EEG similarly targets portable and wearable deployment [22]. These studies compare proposed architectures against baselines, but they do not ask whether gains arise from architectural mechanisms, larger parameter budgets, training recipes, or benchmark saturation. Despite the architectural progression, no systematic study has examined the minimum capacity required for standard EEG denoising benchmarks or whether reconstruction metrics predict downstream task utility.

2.2 Efficiency, Scaling, and Capacity Analysis

Efficiency-aware modeling is well established in EEG classification and broader neural-network design. EEGNet showed that depthwise and separable convolutions can produce compact EEG classifiers across BCI paradigms [23], while MobileNets, Xception, ECA-Net, and deep compression established efficient convolution, attention, pruning, and quantization patterns for low-compute models [24, 25, 26, 27]. Classical online cleaning and preprocessing pipelines such as artifact subspace reconstruction and PREP also reflect deployment-oriented EEG practice [11, 12, 28]. In denoising, compressed and lightweight approaches exist [29, 20, 21], but most studies still emphasize new modules or reconstruction gains rather than controlled capacity.

The capacity question connects directly to broader scaling and over-parameterization theory. Neural scaling laws show that model size, data, and compute can follow predictable performance trends [30], while the lottery ticket hypothesis shows that sparse subnetworks can match dense networks when trained appropriately [31]. These literatures treat capacity as an experimental variable. EEG denoising has not: the field has lacked a capacity-controlled sweep that asks how little model is sufficient for the benchmark.

2.3 Semi-Synthetic Benchmarks and Their Assumptions

EEGDenoiseNet is the de facto benchmark for supervised single-channel EEG denoising [1]. It contains 4514 clean EEG segments, 3400 ocular artifact segments, and 5598 muscular artifact segments sampled at 512 Hz. Noisy examples are generated semi-synthetically by linearly mixing clean EEG with artifact segments at controlled signal-to-noise ratios, allowing each contaminated input to be paired with a clean reference target. This construction makes it possible to report standardized reconstruction metrics such as correlation coefficient and relative root mean square error across EOG and EMG artifact conditions.

Its controlled design has made EEGDenoiseNet widely adopted by subsequent work, including DeepSeparator [20], Denosieformer [19], CT-DCENet [4], DenoiseMamba [5], and MicroWaveNet [21]. The same design encodes a key assumption: segments labeled as “clean” are treated as ground truth, although in practice clean EEG reflects quality-control and preprocessing decisions rather than direct access to artifact-free neural sources [32, 13, 14]. This assumption is appropriate for standardized reconstruction benchmarking, but it limits what reconstruction metrics alone can establish about functional signal utility.

Real-artifact corpora expose the complementary problem. The Temple University Hospital EEG corpus provides clinical recordings with real, heterogeneous artifact conditions [33], but such recordings generally lack paired clean-reference targets, making them incompatible with standard supervised reconstruction evaluation. This gap between the benchmarks the field uses and the conditions it must ultimately address motivates downstream task-aware validation alongside clean-reference metrics.

3 Methods

3.1 Architecture

We model single-channel EEG denoising as a supervised reconstruction problem. Throughout this paper, lowercase letters denote the model-level signals where: $x \in \mathbb{R}^T$ is the assumed-clean EEG segment, $a \in \mathbb{R}^T$ the artifact contribution, and $y = x + a$ the contaminated input. Uppercase letters Y , X , and A denote the corresponding stored arrays. All signals are normalized by the standard deviation of the contaminated signal, $\sigma_y = \text{std}(y)$. The denoiser $f_{\theta, C}$ maps y to a clean estimate $\hat{x} = f_{\theta, C}(y)$, where C is the base channel width.

The architecture used for the width sweep is the controlled backbone shown in Figure 1. The backbone is intentionally minimal: a standard depthwise-separable convolutional U-Net with efficient channel attention, designed to isolate channel capacity as the sole experimental variable rather than to propose a new architecture. To ensure that only channel capacity varied across experimental conditions, the backbone uses a single clean-output head without auxiliary branches or losses. It is a one-dimensional U-Net-like temporal encoder–decoder built from depthwise-separable convolution blocks with efficient channel attention (ECA), following efficient

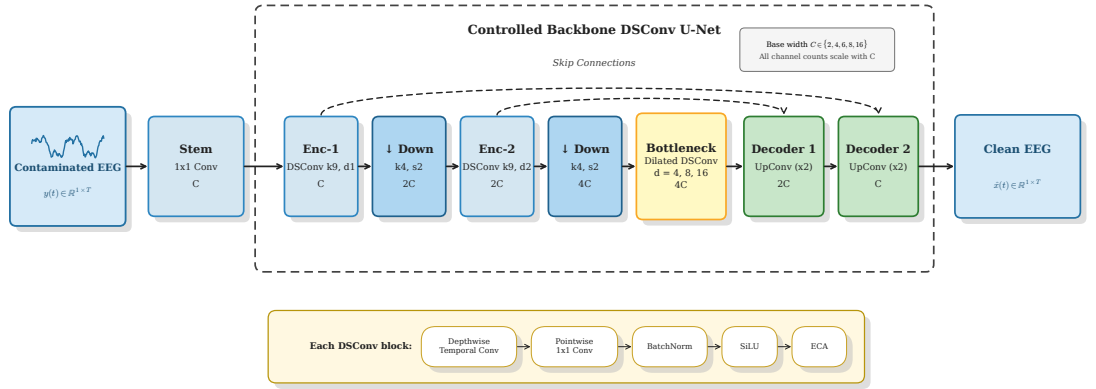


Figure 1. Architecture of the clean-only depthwise-separable convolutional denoiser. The base width C sets the channel count in the stem, encoder, bottleneck, and decoder. The final width-sweep model uses two downsampling stages, a dilated bottleneck, symmetric decoder stages, skip connections, and ECA attention within depthwise-separable convolution blocks.

convolution and lightweight channel-attention design principles [24, 26]. The model takes an input tensor of shape $1 \times T$ and produces one output channel, \hat{x} .

The controlled backbone design was motivated by an additive component study (Supplementary Table S11, Supplementary Figure S6a). Among four variants at 40.24–40.26K parameters, only ECA attention provided a small improvement ($\Delta = +0.005$ CC on EMG, $n = 3$ seeds), and it is retained as a low-cost channel-attention mechanism. Auxiliary artifact-head, spectral, and mixture losses were neutral or harmful and were excluded to maintain the single-variable controlled design.

The network begins with a 1×1 stem convolution from 1 channel to C channels. The encoder contains two depthwise-separable convolution blocks and two strided downsampling convolutions. The first encoder block maps $C \rightarrow C$ with kernel size 9 and dilation 1. The first downsampling layer is a bias-free convolution with kernel size 4, stride 2, and padding 1, mapping $C \rightarrow 2C$. The second encoder block maps $2C \rightarrow 2C$ with kernel size 9 and dilation 2. The second downsampling layer has the same kernel, stride, and padding and maps $2C \rightarrow 4C$. The bottleneck contains three depthwise-separable convolution blocks at width $4C$, with kernel size 9 and dilations 4, 8, and 16. The decoder upsamples with two bias-free transposed convolutions, each using kernel size 4, stride 2, and padding 1. The first maps $4C \rightarrow 2C$, is concatenated with the corresponding $2C$ encoder skip feature, and is followed by a $4C \rightarrow 2C$ depthwise-separable block with dilation 2. The second maps $2C \rightarrow C$, is concatenated with the C -channel encoder skip, and is followed by a $2C \rightarrow C$ block with dilation 1. A final 1×1 convolution maps $C \rightarrow 1$. All depthwise-separable blocks use batch normalization, Sigmoid Linear Unit (SiLU) activation, ECA attention, and an identity residual connection only when the input and output channel counts match.

For an input feature map $H \in \mathbb{R}^{C_{\text{in}} \times T}$, the depthwise-separable convolution first applies a depthwise temporal convolution independently to each channel,

$$u_i(t) = \sum_{r=0}^{k-1} w_{i,r}^{\text{dw}} H_i(t + d(r - \lfloor k/2 \rfloor)), \quad (1)$$

where $k = 9$ and d is the block dilation. A pointwise convolution then mixes channels,

$$v_j(t) = \sum_{i=1}^{C_{\text{in}}} w_{j,i}^{\text{pw}} u_i(t). \quad (2)$$

The block output before residual addition is

$$z = \text{ECA}(\text{SiLU}(\text{BN}(v))). \quad (3)$$

ECA computes a channel descriptor by global temporal averaging,

$$s_c = \frac{1}{T} \sum_{t=1}^T z_c(t), \quad (4)$$

applies a one-dimensional convolution of kernel size 3 along the channel axis, and gates the features with a sigmoid:

$$g = \sigma(\text{Conv1D}_{k=3}(s)), \quad \tilde{z}_c(t) = g_c z_c(t). \quad (5)$$

3.2 Width Parameterization

For the controlled-backbone, the base width C controls every channel dimension in the encoder, bottleneck, and decoder. We evaluated $C \in \{2, 4, 6, 8, 10, 12, 16\}$, producing models with 1.05K, 3.22K, 6.53K, 10.99K, 16.59K, 23.34K, and 40.26K trainable parameters, respectively. Because the depth, kernel sizes, dilation schedule, attention kernel, normalization, activation function, optimizer, and loss were fixed, this family isolates the effect of channel capacity.

3.3 Datasets

3.3.1 EEGDenoiseNet benchmark We used the EEGDenoiseNet semi-synthetic benchmark protocol [1]. For EOG contamination, the prepared dataset contains 27,200 training, 3,400 validation, and 3,400 test segments. Each segment has $T = 512$ samples at 256 Hz. The split is 80/10/10 before expansion, with 3,400 clean EEG and 3,400 EOG segments mixed across 10 SNR levels from -7 to 2 dB. For EMG contamination, the prepared dataset contains 53,736 training, 6,708 validation, and 6,732 test segments. Each segment has $T = 1024$ samples at 512 Hz. The EMG preparation uses 4,514 EEG segments and 5,598 EMG segments, reusing EEG as needed to match the artifact pool, with 12 SNR levels from -7 to 4 dB.

For all semi-synthetic datasets, the mixture coefficient was chosen from the desired SNR r as

$$\lambda = \sqrt{\frac{P_x}{P_a 10^{r/10}}}, \quad y = x + \lambda a, \quad (6)$$

where P_x and P_a are the mean squared powers of the clean and artifact segments.

3.3.2 Large-scale mixed-artifact corpus The mixed-artifact corpus contains 1,000,000 segments at 256 Hz, each with $T = 512$ samples. It was generated from EEGDenoiseNet source pools: 4,514 clean EEG segments of 512 samples, 3,400 EOG artifact segments of 512 samples, and 5,598 EMG artifact segments of 1,024 samples downsampled from 512 Hz to 256 Hz. Source-level splitting was performed before any mixing: clean EEG, EOG, and EMG source indices were assigned to disjoint train, validation, and test pools, preventing source segments from appearing in more than one split. The final dataset contains 800,000 training, 100,000 validation, and 100,000 test mixtures, stored as 80, 10, and 10 chunks of 10,000 segments. The mixed-1M corpus uses the same underlying EEG and artifact source pools as EEGDenoiseNet but substantially extends the evaluation challenge: it introduces multi-artifact mixtures (EOG+EMG, line noise, ECG, electrode drift) not present in the original benchmark, a harder SNR distribution with 30% of segments below -7 dB, stochastic amplitude scaling, and $10\times$ more test segments for tighter statistical estimation. Results on this corpus test robustness to compositional artifact complexity and more adverse noise conditions within the same source distribution.

SNRs were sampled from a two-part distribution: 70% of mixtures used $\text{SNR} \sim \mathcal{U}[-7, 2]$ dB and 30% used $\text{SNR} \sim \mathcal{U}[-12, -7]$ dB. Seven artifact recipes were sampled with fixed probabilities: EOG (0.25), EMG (0.25), EOG+EMG (0.20), EMG+LINE (0.10), EOG+LINE (0.10), EOG+EMG+LINE (0.05), and EOG+EMG+LINE+ECG (0.05). EOG segments were polarity-flipped with probability 0.5 and pre-scaled by $\mathcal{U}[0.7, 1.3]$; EMG segments were pre-scaled by $\mathcal{U}[0.6, 1.5]$. Electrode noise was added with probability 0.35. Line noise used a 50 Hz sinusoid with probability 0.85 and a 60 Hz sinusoid otherwise, with harmonics and slow amplitude modulation. ECG contamination was generated as a synthetic QRS pulse train with an optional T-wave component. After artifact components were combined, the final artifact mixture was scaled to the target SNR.

3.3.3 BCI zero-shot denoising datasets We used BCI Competition IV-2a and IV-2b recordings as zero-shot denoising tests [34]. This protocol is not downstream classification. Real BCI EEG provides the assumed-clean target, real BCI EOG provides the artifact template, and known-SNR mixtures are generated so reconstruction metrics can be computed.

For BCI IV-2a, we used subject A01T, EEG channel index 9, and EOG channel index 22. The recording was resampled from 250 Hz to 256 Hz. Clean windows were drawn from the lowest 20% of EOG-band energy and artifact windows from the highest 10%, giving 2,148 clean starts and 1,074 artifact starts. For BCI IV-2b, we used B0101T, EEG:C3, and EOG:ch01, giving 1,934 clean

starts and 967 artifact starts after the same selection rule. For each dataset, 5,000 test mixtures were generated with seed 42 and SNR uniformly sampled from $[-6, 2]$ dB.

3.4 Training Protocol

All width variants were trained with AdamW, initial learning rate 10^{-3} , weight decay 10^{-4} , gradient clipping at norm 1.0, and checkpoint selection by validation SDR. EEGDenoiseNet EOG and EMG width-sweep runs used 25 epochs, batch size 256, two data-loading workers, and a 3-epoch linear warm-up followed by cosine decay. Mixed-1M runs used 10 epochs, batch size 1024, two workers, and a 2-epoch linear warm-up followed by cosine decay. The main multi-seed experiments used seeds 42, 43, and 44. For the final EEGDenoiseNet Pareto-width statistical aggregation, base2, base4, base6, base8, and base16 were additionally trained with seeds 45 and 46, giving five seeds $\{42, 43, 44, 45, 46\}$ for those widths. Base10 and base12 remained exploratory $n = 3$ widths.

The training objective was clean reconstruction only:

$$\mathcal{L}_x = \frac{1}{T} \sum_{t=1}^T \sqrt{(\hat{x}(t) - x(t))^2 + \epsilon_H^2}, \quad \epsilon_H = 2 \times 10^{-3}. \quad (7)$$

The pseudo-Huber form with $\epsilon_H = 2 \times 10^{-3}$ transitions smoothly from L2 behaviour for small residuals to L1 behaviour for large residuals, providing smooth gradients near zero while maintaining robustness to outliers [35]. Auxiliary artifact, mixture-consistency, spectral, and envelope losses were set to zero for the width-sweep experiments.

All full training and profiling runs were executed on the AI Lab workstation with an AMD EPYC 7313 16-core CPU, 32 logical threads, an NVIDIA RTX A5000 GPU with 24,564 MiB memory, PyTorch 2.10.0+cu128, and CUDA 12.8.

3.5 Evaluation Metrics

Let \hat{x} be the denoised estimate and x the assumed-clean reference. Correlation coefficient (CC) was computed after temporal mean removal:

$$\text{CC}(x, \hat{x}) = \frac{\sum_{t=1}^T (x_t - \bar{x})(\hat{x}_t - \bar{\hat{x}})}{\sqrt{\sum_{t=1}^T (x_t - \bar{x})^2} \sqrt{\sum_{t=1}^T (\hat{x}_t - \bar{\hat{x}})^2}}. \quad (8)$$

Root mean squared error was

$$\text{RMSE}(x, \hat{x}) = \sqrt{\frac{1}{T} \sum_{t=1}^T (x_t - \hat{x}_t)^2}. \quad (9)$$

Temporal relative RMSE was

$$\text{T-RRMSE}(x, \hat{x}) = \frac{\|x - \hat{x}\|_2}{\|x\|_2}. \quad (10)$$

For spectral metrics, Welch power spectral densities $P_x(f)$ and $P_{\hat{x}}(f)$ were estimated with $n_{\text{perseg}} = \min(256, T)$. Spectral relative RMSE was

$$\text{S-RRMSE}(x, \hat{x}) = \frac{\|P_x - P_{\hat{x}}\|_2}{\|P_x\|_2}. \quad (11)$$

Signal-to-distortion ratio was

$$\text{SDR}(x, \hat{x}) = 10 \log_{10} \frac{\sum_{t=1}^T x_t^2 + \epsilon}{\sum_{t=1}^T (x_t - \hat{x}_t)^2 + \epsilon}. \quad (12)$$

In both SDR and PSD-KLD, $\epsilon = 10^{-10}$ serves as a numerical stabilization constant. For PSD-KLD, PSDs were normalized to probability vectors $p_x(f)$ and $p_{\hat{x}}(f)$, and

$$\text{PSD-KLD}(x, \hat{x}) = \sum_f p_x(f) \log \frac{p_x(f) + \epsilon}{p_{\hat{x}}(f) + \epsilon}. \quad (13)$$

3.6 Downstream BCI Classification Protocol

Downstream utility was evaluated on BCI Competition IV-2a using all nine subjects (A01–A09). For each subject, the official A0xT session was used for training and the A0xE session was used as the held-out evaluation session. No cross-validation was used; the protocol followed the fixed train/test split. The first 22 EEG channels were used for classification, and EOG channel index 22 was used only to generate synthetic contamination. Trials labeled as artifacts were excluded. Trials were cropped from 2.5 s to 6.0 s after cue onset and resampled from 250 Hz to 256 Hz, giving 896 samples per trial. EOG-contaminated versions of the training and test trials were generated with SNR uniformly sampled from $[-6, 2]$ dB. The test contamination used seed 42 and the training contamination used seed 1042. For contamination-type robustness, we repeated the CSP+LDA matched denoised/denoised protocol with EOG, EMG, and EOG+EMG+LINE recipes. EOG templates came from the BCI IV-2a EOG channel, EMG templates came from the EEGDenoiseNet raw EMG artifact pool after resampling to 256 Hz, and mixed artifacts combined EOG, EMG, and synthetic 50/60 Hz line noise before global SNR scaling.

We evaluated five decoder families. The classical spatial-filter pipeline used CSP+LDA, a standard linear approach for motor-imagery BCI [36, 37, 38, 39]. This pipeline applied a fourth-order Butterworth bandpass filter from 8 to 30 Hz. CSP used 8 components, Oracle Approximating Shrinkage (OAS) covariance regularization, log-variance features, per-class covariance estimated from time-concatenated trials (rather than averaging per-trial covariance matrices), and no trace normalization. The classifier was LDA with LSQR solver and automatic shrinkage. Because CSP and LDA are linear feature-extraction and classification stages, changes in classification accuracy were interpreted as task-level utility changes rather than as direct localization of neural generators [40, 41].

The remaining four decoders: EEGNet [23], ShallowFBCSPNet, Deep4Net [42], and EEGConformer [43], used official Braindecode implementations [42] and were trained for 80 epochs with AdamW, learning rate 10^{-3} , weight decay 10^{-4} , and batch size 64. A 200-epoch convergence audit is reported in the supplementary material.

For each classifier, we evaluated five train/test conditions: clean/clean, clean/noisy, noisy/noisy, clean/denoised, and denoised/denoised. The clean/denoised condition tests strict preservation under a clean-trained classifier, whereas denoised/denoised tests the matched practical case in which the classifier is trained and tested on the denoiser output. Each of the 22 EEG channels was denoised independently by the single-channel model, matching the single-channel benchmark protocol. To test whether this per-channel application introduces cross-channel covariance effects, we additionally trained multichannel controls (Section 4.4). Statistical significance of the matched denoised/denoised versus noisy/noisy comparison was assessed with one-sided Wilcoxon signed-rank tests across subjects, with the alternative hypothesis that denoised accuracy is lower than noisy/noisy accuracy. To test this single-channel-to-multichannel confound directly, we additionally trained subject-specific 22-channel Depthwise-Separable Convolution (DSConv) U-Net controls at base6 and base16 on the BCI IV-2a training sessions and evaluated matched CSP+LDA on the held-out evaluation sessions. These multichannel controls were used only as downstream diagnostics and were not part of the main single-channel reconstruction benchmark.

3.7 Compute Profiling Methodology

Compute profiling was performed on 512-sample inputs at 256 Hz. FLOPs were computed as $2 \times \text{MACs}$ counted with hooks on Conv1d, ConvTranspose1d, Linear, and LSTM layers. Latency was measured on CPU and CUDA for batch sizes 1 and 256 using 30 warm-up and 100 timed iterations with device synchronization. The full profiling methodology is provided in the supplementary material.

4 Results

Unless stated otherwise, results for our models are reported as mean \pm sample standard deviation over independent training seeds. Mixed-1M and BCI zero-shot evaluations use seeds 42, 43, and 44; the final EEGDenoiseNet Pareto widths use seeds 42–46. Published external baselines are reported as single reference values.

4.1 Reconstruction Performance Saturates Early

The lower-anchor baselines show that EEGDenoiseNet requires learning, but not large capacity. Zero-parameter filters reached at most EOG CC 0.552 and EMG CC 0.743, a 34-parameter learned FIR reached 0.784/0.779, and a 365-parameter tiny TCN reached 0.849/0.797 (Supplementary

Table 1. EEGDenoiseNet benchmark comparison. Width-variants base2/base4/base6/base8/base16 of the controlled depthwise-separable U-Net backbone are $n=5$ results from the fixed statistical aggregation; base10/base12 are $n=3$ exploratory widths. EEGDN CNN and MicroWaveNet controlled rows were retrained under our pipeline. Literature rows are published reference values and were not retrained. NR: not reported.

Model	Params	EOG CC	EOG T-RRMSE	EOG S-RRMSE	EMG CC	EMG T-RRMSE	EMG S-RRMSE	Source
base2	1.05K	0.871 ± 0.014	0.496 ± 0.038	0.474 ± 0.051	0.822 ± 0.007	0.539 ± 0.019	0.353 ± 0.033	controlled
base4	3.22K	0.898 ± 0.002	0.426 ± 0.004	0.386 ± 0.009	0.837 ± 0.001	0.503 ± 0.001	0.307 ± 0.004	controlled
base6	6.53K	0.904 ± 0.003	0.412 ± 0.009	0.365 ± 0.009	0.840 ± 0.001	0.497 ± 0.003	0.299 ± 0.005	controlled
base8	10.99K	0.907 ± 0.001	0.402 ± 0.003	0.353 ± 0.003	0.843 ± 0.001	0.492 ± 0.001	0.292 ± 0.003	controlled
base10	16.59K	0.910 ± 0.001	0.396 ± 0.003	0.343 ± 0.005	0.844 ± 0.001	0.490 ± 0.001	0.286 ± 0.001	controlled
base12	23.34K	0.912 ± 0.001	0.391 ± 0.002	0.336 ± 0.002	0.844 ± 0.000	0.489 ± 0.000	0.283 ± 0.001	controlled
base16	40.26K	0.915 ± 0.001	0.385 ± 0.002	0.320 ± 0.005	0.843 ± 0.002	0.491 ± 0.003	0.285 ± 0.009	controlled
EEGDN CNN (controlled)	8.46M/33.62M	0.915 ± 0.002	0.374 ± 0.004	0.317 ± 0.001	0.789 ± 0.002	0.606 ± 0.004	0.376 ± 0.006	controlled
MicroWaveNet (controlled)	53.50K	0.868 ± 0.052	0.481 ± 0.095	0.432 ± 0.085	0.799 ± 0.003	0.561 ± 0.003	0.365 ± 0.002	controlled
EEGDN CNN (published)	8.40M	0.923	0.336	0.343	0.786	0.632	0.604	literature
EEGDN RNN (published)	787.0K	0.900	0.411	0.389	0.816	0.561	0.521	literature
CT-DCENet (published)	38.10M	0.947	0.246	NR	0.933	0.304	NR	literature
DeepSeparator (published)	32.00K	0.769	0.705	0.747	0.734	0.712	0.717	literature
MicroWaveNet (published)	60.00K	0.910	0.378	0.404	0.830	0.467	0.389	literature

Base10 and base12 were evaluated on EEGDenoiseNet only and are omitted from subsequent mixed-artifact, transfer, compute, and downstream analyses for clarity. Rows marked controlled were retrained under our data split, loss, and metric pipeline; rows marked published are point estimates from the original papers and were not rerun. The controlled EEGDN CNN parameter count differs between EOG and EMG because the dense output head scales with segment length. Controlled MicroWaveNet uses our pseudo-Huber loss and pipeline; the original multi-loss Soft-DTW and wavelet-domain recipe was not reproduced. CT-DCENet values are from the original publication; no public code is available for independent verification.

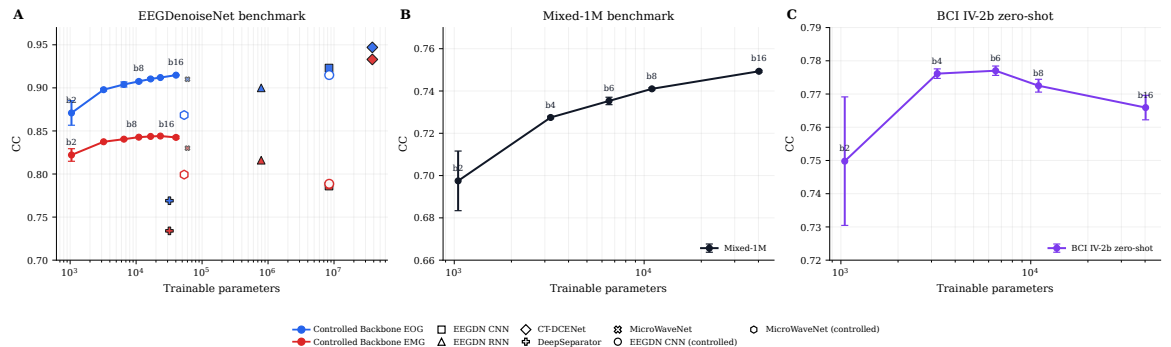


Figure 2. Pareto frontier across reconstruction benchmarks. Panel A shows EEGDenoiseNet EOG and EMG CC versus parameter count, Panel B shows Mixed-1M CC, and Panel C shows BCI IV-2b zero-shot CC. Controlled backbone variants are shown as connected width-sweep points, and external baselines are shown as reference markers. Parameter count is shown on a log scale.

Table 2. Mixed-1M multi-seed results.

Base	Params	CC	RMSE	T-RRMSE	S-RRMSE	SDR
2	1.05K	0.698 ± 0.014	0.233 ± 0.012	0.697 ± 0.024	0.631 ± 0.029	3.59 ± 0.37
4	3.22K	0.728 ± 0.001	0.209 ± 0.001	0.645 ± 0.001	0.573 ± 0.006	4.44 ± 0.02
6	6.53K	0.735 ± 0.002	0.205 ± 0.000	0.633 ± 0.002	0.560 ± 0.002	4.64 ± 0.03
8	10.99K	0.741 ± 0.001	0.202 ± 0.000	0.624 ± 0.001	0.547 ± 0.002	4.79 ± 0.02
16	40.26K	0.749 ± 0.001	0.196 ± 0.000	0.611 ± 0.001	0.534 ± 0.004	5.05 ± 0.01

Table S3). The controlled width sweep then pushed reconstruction into the benchmark-saturating regime with only a few thousand parameters.

On EEGDenoiseNet, most reconstruction gain appeared below 10K parameters (Table 1; Figure 2A). Base8 reached EOG CC 0.907 ± 0.001 with 10.99K parameters, while base16 reached 0.915 ± 0.001 with 40.26K parameters. EMG saturated earlier: base6–base16 differed by only 0.003 CC. A segmented regression of CC against \log_{10} parameter count selected base4 as the descriptive elbow for both EOG and EMG. The post-elbow slope was 0.0151 CC per \log_{10} -parameter unit for EOG and 0.0044 for EMG, with the EMG bootstrap interval including zero (-0.0003 to 0.0056). Supplementary Table S1 gives the fixed $n = 5$ statistics, Supplementary Table S5 gives the knee-fit details, and Supplementary Figure S3 gives the full relative-error curves.

The EEGDenoiseNet results establish the ceiling on the primary single-artifact benchmark; the next question is whether the saturation pattern persists under multi-artifact compositional complexity, harder SNR conditions, and larger test-set scale. The same saturation pattern held on the larger mixed-artifact corpus (Table 2; Figure 2B). Base4 reached 0.728 ± 0.001 , base8 reached 0.741 ± 0.001 , and base16 added a further 0.008 CC at more than three times the parameter count. Supplementary Figure S1 shows the per-seed scatter plots.

To test whether the ceiling extends beyond the training distribution, we evaluated all width variants on BCI Competition IV recordings without fine-tuning. Zero-shot BCI transfer preserved the early-saturation pattern but showed dataset-dependent capacity effects (Table 3). BCI IV-2a

Table 3. BCI zero-shot multi-seed results.

Dataset	Base	Params	CC	RMSE	T-RRMSE	S-RRMSE	SDR
IV-2a	2	1.05K	0.702 ± 0.017	0.471 ± 0.015	0.731 ± 0.023	0.796 ± 0.022	2.81 ± 0.29
IV-2a	4	3.22K	0.726 ± 0.004	0.446 ± 0.003	0.693 ± 0.005	0.736 ± 0.013	3.30 ± 0.07
IV-2a	6	6.53K	0.731 ± 0.004	0.440 ± 0.003	0.684 ± 0.004	0.712 ± 0.005	3.42 ± 0.06
IV-2a	8	10.99K	0.735 ± 0.003	0.437 ± 0.003	0.681 ± 0.004	0.694 ± 0.011	3.47 ± 0.06
IV-2a	16	40.26K	0.736 ± 0.004	0.436 ± 0.003	0.678 ± 0.004	0.673 ± 0.014	3.50 ± 0.06
IV-2b	2	1.05K	0.750 ± 0.019	0.426 ± 0.020	0.674 ± 0.030	0.545 ± 0.051	3.59 ± 0.41
IV-2b	4	3.22K	0.776 ± 0.001	0.398 ± 0.002	0.632 ± 0.003	0.459 ± 0.011	4.18 ± 0.04
IV-2b	6	6.53K	0.777 ± 0.001	0.397 ± 0.002	0.630 ± 0.002	0.447 ± 0.002	4.20 ± 0.03
IV-2b	8	10.99K	0.772 ± 0.002	0.401 ± 0.002	0.637 ± 0.004	0.451 ± 0.004	4.12 ± 0.05
IV-2b	16	40.26K	0.766 ± 0.004	0.408 ± 0.003	0.647 ± 0.004	0.455 ± 0.006	3.98 ± 0.06

improved gradually through base16, whereas BCI IV-2b peaked at base6 and then declined (Figure 2C). The IV-2b inversion, base6 > base8 > base16, indicates that additional reconstruction capacity can reduce transfer performance.

Finally, we examined whether input difficulty or artifact type interacts with the saturation pattern. SNR and artifact stratification show that input difficulty affects absolute CC more than width affects the ceiling (Supplementary Figure S6b, S6c). Width ordering was preserved across SNR bins, with base2 separated most clearly at the lowest SNRs. Artifact type dominated recipe difficulty: EOG-only rows formed a high-CC band, whereas EMG-containing recipes formed a lower-CC band with little left-to-right gradient across widths.

4.2 Controlled Baselines Confirm the Ceiling Is Not Architecture-Specific

Controlled same-pipeline retraining shows that the ceiling is not simply an artifact of comparing against weak baselines. EEGDN CNN matched base16 on EOG with CC 0.915 ± 0.002 , but required 8.46M parameters for the 512-sample EOG setting. On EMG, EEGDN CNN reached only 0.789 ± 0.002 , below all controlled backbone widths (Table 1; Supplementary Table S2).

Controlled MicroWaveNet retraining also fell below the compact operating range of the controlled backbone under the same split, loss, and metric pipeline (Supplementary Table S2). This same-pipeline comparison isolates architectural capacity from training-recipe effects, which is precisely the controlled design this study requires.

A second-family Patch-Transformer sweep showed the same diminishing-return pattern in a non-U-Net architecture. Increasing from 1.35K to 4.87K parameters gave large gains, whereas the 40.71K-parameter variant reached EOG CC 0.891 ± 0.001 and EMG CC 0.831 ± 0.001 , below base16 under the same training pipeline (Supplementary Table S4). This control reduces the concern that early saturation is unique to depthwise-separable U-Nets.

The remaining entries in Table 1 are literature reference values reported under each method’s original evaluation protocol, since publicly available code was not released for most of these models. CT-DCENet reports EOG CC 0.947 with 38.10M parameters [4], but its evaluation protocol (normalization domain, test-split construction, data augmentation, optimization budget) is not independently verifiable. Even accepting the reported value, a roughly 1000× parameter increase over base16 yields a 3.2-point CC improvement on EOG – a marginal gain that reinforces rather than contradicts the diminishing-return pattern. The controlled same-pipeline evidence is more informative: EEGDN CNN at 8.46M parameters matched base16 on EOG, MicroWaveNet did not exceed the compact variants, and the Patch-Transformer showed the same saturation shape. These results support the conclusion that standard benchmarks can be largely saturated by compact temporal models under controlled conditions.

4.3 Deployment Profiling

The compact Pareto widths occupy deployment-relevant size and compute regimes (Table 4; Figure 3). Base4–base6 require 33.3–45.8 KB on disk and 1.27–2.61M FLOPs per 512-sample segment. Base16 improves reconstruction modestly but increases size to 179.8 KB and FLOPs to 16.30M.

4.4 Reconstruction Metrics Do Not Predict Downstream Task Utility

4.4.1 Baseline Conditions and Experimental Design CSP+LDA provided the strongest noisy/noisy baseline among the five downstream decoders (0.612 ± 0.173), making it the primary test of whether denoising preserves task-relevant motor-imagery structure (Supplementary Table S6). Because the denoisers are single-channel models applied independently to the 22 EEG

Table 4. Compute profile on 512-sample inputs. CPU latency is batch-1 mean latency. GPU throughput and peak memory are measured at batch size 256.

Model	Params	FLOPs/segment	Size KB	CPU ms	GPU throughput/s	GPU peak KB
base2	1.05K	0.40M	24.3	1.49	181 760	14 881
base4	3.22K	1.27M	33.3	1.58	177 146	29 223
base6	6.53K	2.61M	45.8	1.63	165 138	43 572
base8	10.99K	4.42M	64.4	1.73	160 815	57 924
base16	40.26K	16.30M	179.8	2.10	99 865	115 381
EEGDN CNN	8.46M	83.00M	33 079	2.68	34 249	157 642
EEGDN RNN	787.0K	1.58M	3 082	0.42	653 361	34 443

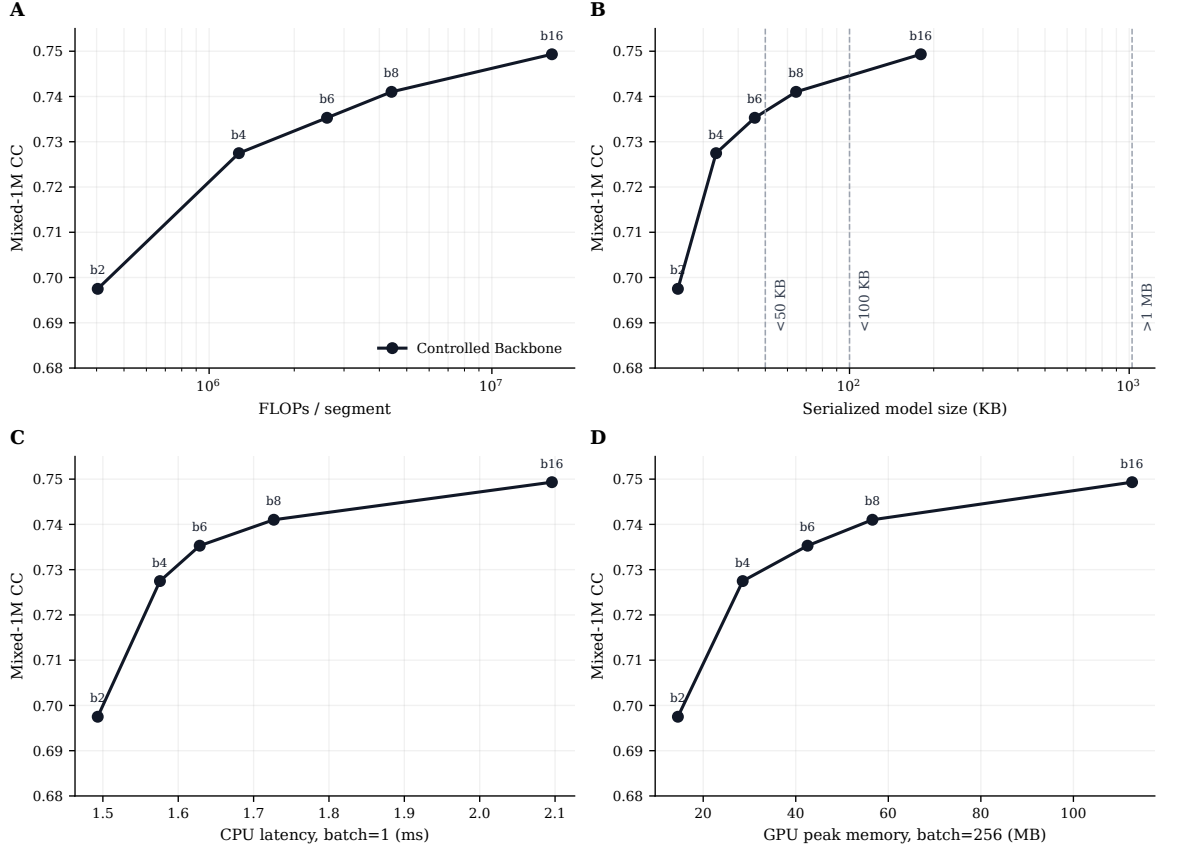


Figure 3. Compute efficiency Pareto plots. Panels show CC versus FLOPs, serialized model size, CPU inference latency, and GPU peak memory.

channels, the downstream protocol also tests whether high reconstruction fidelity survives the cross-channel covariance requirements of spatial-filter classifiers.

4.4.2 The Classifier-Dependent Utility Gap Denoising harmed spatial-filter pipelines most strongly (Table 5; Figure 4). CSP+LDA was below noisy/noisy for all widths, and the best matched denoised/denoised condition remained 0.065 below baseline. This comparison survived correction across the five best-width classifier tests. ShallowFBCSPNet also decreased at its best denoised width, but the result did not survive Bonferroni correction. EEGConformer, EEGNet, and Deep4Net showed non-significant or neutral effects, producing a gradient from spatial-filter sensitivity to end-to-end decoder adaptability. The full width-by-classifier matrix is provided in Supplementary Table S7, per-checkpoint CSP+LDA diagnostics are shown in Supplementary Figure S4, and Figure 5 summarizes the corresponding deltas.

4.4.3 The Gap Is Not Artifact-Specific The CSP+LDA gap persisted across artifact recipes (Table 6). The EOG row anchors this analysis to the main synthetic-EOG CSP+LDA results from Table 5, while EMG and mixed EOG+EMG+LINE contamination produced larger reduction. All nine subjects were below the noisy/noisy baseline at the best fixed width for EMG and mixed contamination.

4.4.4 The Gap Persists on Real Recordings The utility gap also appeared when denoisers were applied directly to naturally recorded BCI IV-2a trials without synthetic artifact injection

Table 5. Best matched denoised/denoised downstream BCI IV-2a result for each classifier. Accuracy and deltas are mean \pm standard deviation across nine subjects. Wilcoxon p -values compare matched denoised/denoised accuracy against the noisy/noisy baseline with the one-sided alternative that denoised accuracy is lower. Bonferroni and Benjamini–Hochberg false-discovery-rate (BH-FDR) corrections are applied across the five best-width classifier comparisons.

Classifier	Best fixed width	Accuracy	Δ vs noisy/noisy	p	Bonf. p	BH q
CSP+LDA	base16	0.547 ± 0.174	-0.065 ± 0.060	0.0098	0.0488	0.0488
ShallowFBCSPNet	base16	0.477 ± 0.155	-0.019 ± 0.025	0.0273	0.1367	0.0684
EEGConformer	base8	0.469 ± 0.159	-0.015 ± 0.045	0.1797	0.8984	0.2995
EEGNet	base6	0.417 ± 0.129	-0.006 ± 0.056	0.2480	1.0000	0.3101
Deep4Net	base16	0.409 ± 0.132	$+0.018 \pm 0.050$	0.8496	1.0000	0.8496

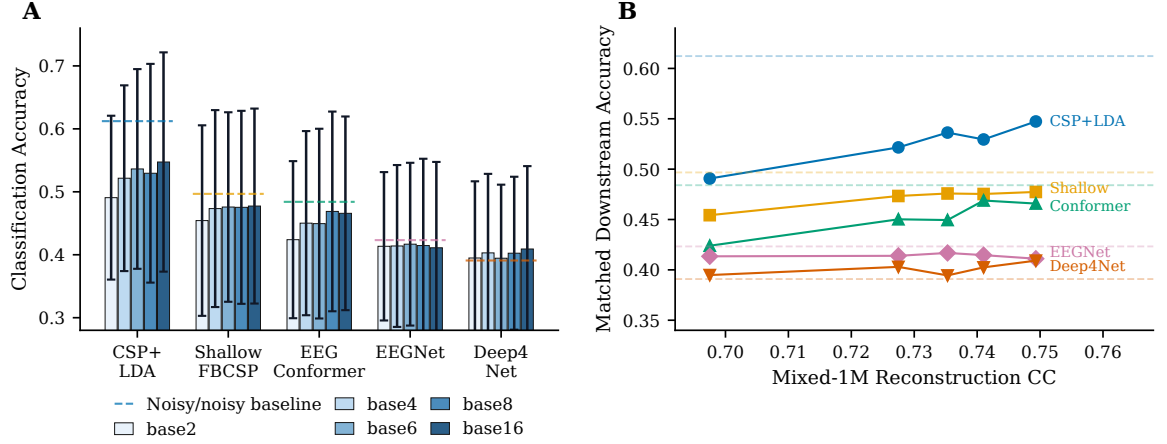


Figure 4. Downstream BCI utility gap across classifier families. Panel A shows matched denoised/denoised classification accuracy for each width variant and each classifier, with classifier-specific noisy/noisy baselines indicated by dashed horizontal reference segments. Error bars denote standard deviation across the nine BCI IV-2a subjects, and significance markers above the best fixed width indicate one-sided Wilcoxon tests against noisy/noisy (**: $p < 0.01$, *: $p < 0.05$, n.s.: not significant). Panel B plots Mixed-1M reconstruction CC against matched denoised/denoised downstream accuracy for all width variants and classifiers; dashed horizontal lines show classifier-specific noisy/noisy baselines.

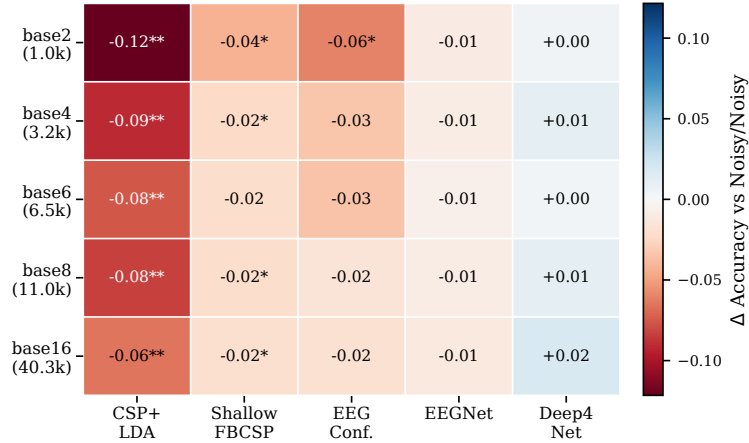


Figure 5. Width \times classifier utility-gap heatmap. Each cell shows the change in matched denoised/denoised classification accuracy relative to the noisy/noisy baseline, averaged across all nine BCI IV-2a subjects. Negative values indicate denoising-induced degradation; positive values indicate improvement. Significance markers denote one-sided Wilcoxon signed-rank tests against noisy/noisy (**: $p < 0.01$, *: $p < 0.05$, uncorrected).

Table 6. CSP+LDA downstream robustness across synthetic artifact recipes. Values are mean \pm standard deviation across nine BCI IV-2a subjects. Wilcoxon p -values compare the best matched denoised/denoised condition against noisy/noisy with the one-sided alternative that denoised accuracy is lower.

Contaminant	Noisy/noisy	Best width	Best denoised/denoised	Δ vs noisy/noisy	p / BH q
EOG	0.612 ± 0.173	base16	0.547 ± 0.174	-0.065 ± 0.060	0.0098 / 0.0098
EMG	0.613 ± 0.164	base6	0.504 ± 0.169	-0.109 ± 0.080	0.0020 / 0.0059
EOG+EMG+LINE	0.610 ± 0.166	base4	0.497 ± 0.163	-0.114 ± 0.086	0.0020 / 0.0059

Table 7. Real non-synthetic BCI IV-2a CSP+LDA evaluation. Denoisers were applied directly to recorded trials without synthetic EOG injection. Values are mean \pm standard deviation across nine subjects. BH-FDR q -values correct the matched denoised/denoised comparisons across widths.

Condition	Width	Accuracy	Δ vs raw/raw	BH-FDR q
raw/raw	–	0.643 \pm 0.160	–	–
denoised/denoised	base2	0.544 \pm 0.146	–0.100 \pm 0.051	0.0049
denoised/denoised	base4	0.583 \pm 0.166	–0.060 \pm 0.040	0.0049
denoised/denoised	base6	0.593 \pm 0.180	–0.051 \pm 0.052	0.0059
denoised/denoised	base8	0.597 \pm 0.178	–0.047 \pm 0.038	0.0049
denoised/denoised	base16	0.594 \pm 0.183	–0.049 \pm 0.044	0.0049

Table 8. Multichannel denoiser control for CSP+LDA downstream evaluation. Single-channel rows apply the denoiser independently to each EEG channel. Multichannel control rows use subject-specific 22-channel DSConv U-Net denoisers trained on the BCI IV-2a training session. Values are mean \pm standard deviation across nine subjects.

Scope	Width	Params	Accuracy	Δ vs noisy/noisy	Subjects below	p / BH q
Noisy/noisy baseline	–	–	0.612 \pm 0.173	–	–	–
Single-channel	base6	6.53K	0.536 \pm 0.159	–0.076 \pm 0.068	7/9	0.0098 / 0.0130
Single-channel	base16	40.26K	0.547 \pm 0.174	–0.065 \pm 0.060	7/9	0.0098 / 0.0130
Multichannel control	base6	88.87K	0.513 \pm 0.163	–0.100 \pm 0.078	7/9	0.0098 / 0.0130
Multichannel control	base16	602.99K	0.567 \pm 0.174	–0.045 \pm 0.076	6/9	0.0645 / 0.0645

(Table 7). The best matched denoised CSP+LDA condition was base8 at 0.597 \pm 0.178, below raw/raw by 4.7 percentage points, and all matched denoised widths were significant after BH-FDR correction. This result shows that the spatial-filter gap is not an artifact of the synthetic contamination protocol.

4.4.5 The Gap Is Not Explained by Independent-Channel Processing Because the controlled backbone is a single-channel denoiser applied independently to 22 EEG channels, it may distort the cross-channel covariance structure that CSP+LDA depends on. To isolate this confound, we trained subject-specific 22-channel DSConv U-Net denoisers at base6 and base16 on the BCI IV-2a training sessions and evaluated matched CSP+LDA on the held-out evaluation sessions (Table 8).

Multichannel base16 reduced the gap relative to single-channel denoising ($\Delta = -0.045$ versus -0.065), but multichannel base6 produced a larger reduction ($\Delta = -0.100$). Even the best multichannel condition did not reach the noisy/noisy baseline. Covariance-aware denoising partially mitigates but does not eliminate the utility gap, confirming that both amplitude suppression and cross-channel distortion contribute independently to the downstream degradation.

4.4.6 Calibration and Convergence Controls Post-denoising train-channel z-scoring, raw-variance rescaling, and covariance recoloring did not recover noisy/noisy performance; per-trial z-scoring reduced the average gap but remained below baseline (Supplementary Table S8). A 200-epoch convergence audit improved Deep4Net and EEGConformer noisy/noisy baselines, but their denoising effects remained statistically inconclusive (Supplementary Table S9). Supplementary Tables S6–S10 provide the full downstream archive, including baseline, width-matrix, calibration, convergence, and task-aware pilot summaries. These controls indicate that the utility gap is not explained by simple calibration failure or neural-decoder under-training.

4.4.7 Qualitative Mechanism: Amplitude Suppression in Quiet Intervals Real-artifact examples provide a mechanism for the downstream results (Supplementary Figure S7). In high-EOG windows, all widths removed most of the blink-scale signal component. In quiet-baseline windows, however, base4–base16 still removed 35–59% of raw RMS depending on dataset, even when visible artifact activity was low. This over-stripping supports an amplitude-suppression mechanism: semi-synthetic reconstruction training can teach the model to treat high-amplitude structure as artifact even when that structure may carry task-relevant neural information. Supplementary Figure S2 shows high-amplitude transient examples, and Supplementary Figure S5 gives the full removed/raw RMS heatmap.

5 Discussion

5.1 Why the Ceiling Exists

The width sweep shows that these benchmarks saturate with compact temporal models. Most reconstruction gain appears below 10K parameters, and the EMG post-elbow slope is statistically indistinguishable from zero under the descriptive bootstrap analysis. Performance continues to

improve marginally at higher widths, but the benchmark mapping becomes easy relative to the capacity added beyond base4–base8, consistent with a low-dimensional separation problem.

A plausible explanation is low-dimensional spectral separation. EOG artifacts are dominated by low-frequency structure, EMG is broadband and overlaps more strongly with neural activity, and line noise is narrowband. The artifact-stratified heatmap supports this mechanism: EMG presence changes difficulty far more than width, while line noise and ECG additions have smaller effects once EMG is present. A compact temporal convolutional model with dilation can learn these coarse temporal and spectral boundaries without requiring millions of parameters.

The BCI IV-2b inversion reinforces this interpretation. Larger models did not produce more transferable denoising; base6 exceeded base16 on that zero-shot transfer setting. Extra capacity can therefore fit training-distribution details rather than learning a more general artifact-removal rule. The Patch-Transformer control shows that early diminishing returns are not unique to the DSConv U-Net template. Uncontrolled literature-reported scores from models without publicly available code cannot isolate whether apparent gains reflect architectural capacity, training-recipe details, or evaluation-protocol differences, and therefore do not contradict the controlled same-pipeline evidence.

5.2 Why Metrics and Utility Diverge

Reconstruction metrics and downstream utility diverge because reconstruction training can remove signal components that classifiers use. As shown in the qualitative analysis (Supplementary Figure S7), denoisers removed substantial signal energy even in quiet-baseline windows, consistent with an amplitude-suppression bias from semi-synthetic training.

The single-channel-to-multichannel interface adds a second mechanism. The controlled backbone denoises each EEG channel independently before spatial-filter classification, while CSP+LDA depends on cross-channel covariance and band-power relationships. However, the controls show that covariance distortion alone is not sufficient to explain the gap. Post-denoising z-scoring, raw-variance rescaling, and covariance recoloring did not recover noisy/noisy performance, and a focused 22-channel multichannel denoiser reduced but did not eliminate the CSP+LDA reduction (Table 8). The utility loss therefore reflects both amplitude suppression and task-relevant representational change.

Classifier architecture determines how strongly this mismatch appears. CSP+LDA is linear and cannot learn compensatory filters after denoising; ShallowFBCSPNet inherits similar band-power sensitivity. End-to-end decoders can partly adapt to the altered signal distribution, which explains why EEGNet, Deep4Net, and EEGConformer showed variable or neutral effects. The 200-epoch audit improved neural-decoder baselines but did not convert denoising into a reliable downstream benefit.

A task-aware pilot tested whether adding frozen CSP-feature preservation to a 22-channel denoiser could close the gap. It did not: the auxiliary loss worsened matched CSP+LDA performance relative to reconstruction-only multichannel denoising, with $\Delta = -0.061$ at $\lambda = 0.1$ and $\Delta = -0.102$ at $\lambda = 1.0$, compared with $\Delta = -0.043$ for reconstruction-only training (Supplementary Table S10). This result demonstrates that closing the metric–utility gap requires more principled task-aware optimization than simple noisy-feature matching, and identifies frozen-feature preservation as an insufficient approach.

The interpretation should be read alongside the standard assumption of supervised EEG denoising: the “clean” reference is itself a preprocessed approximation, not an independently observed artifact-free neural source [32, 28, 13, 14, 7]. This assumption is shared by every method evaluated on EEGDenoiseNet and related benchmarks. Our results therefore characterize the capacity requirements of the evaluation standard the field currently uses, which is the necessary first step toward designing harder benchmarks that better approximate real artifact removal.

5.3 Implications and Recommendations

For practitioners deploying edge EEG, base4–base6 are the practical operating points in this study. They use 3.22K–6.53K parameters, occupy 33–46 KB on disk, and preserve most of the reconstruction performance of larger variants. Million-parameter denoisers should therefore be justified by application-specific improvements in robustness, transfer, or task utility, not by reconstruction metrics alone.

For researchers publishing denoising methods, downstream task evaluation should accompany CC, RMSE, SDR, and spectral-error metrics. The present results show that a denoiser can improve reconstruction while degrading CSP+LDA classification across subjects, artifact types, and

naturally recorded trials. Reconstruction fidelity remains necessary, but it should be treated as an intermediate diagnostic rather than a complete success criterion.

For benchmark designers, the next step is to move beyond semi-synthetic clean-reference mixtures alone. The Temple University Hospital EEG corpus provides clinical recordings with real, heterogeneous artifacts [33], but it lacks paired clean targets. Future benchmarks should combine realistic artifact conditions with task-aware endpoints such as motor-imagery decoding, ERP detection, seizure-marker preservation, or spectral biomarker stability.

For loss-function designers, task-aware denoising is promising but technically delicate. Recent task-oriented denoising proposals point in this direction [44], but our CSP-feature pilot shows that naive feature preservation can worsen downstream performance. Three directions appear more viable than frozen-feature matching. First, differentiable end-to-end pipelines that backpropagate classifier gradients through the denoiser could jointly optimize reconstruction fidelity and task utility, avoiding the proxy mismatch of separately trained objectives. Second, band-selective or spectrally constrained losses that explicitly penalize attenuation in task-relevant frequency bands (e.g., 8–30 Hz mu/beta for motor imagery, 1–4 Hz delta for sleep staging) could reduce neural feature suppression without requiring a full downstream classifier during training. Third, multi-objective Pareto training that treats reconstruction and downstream preservation as competing objectives could identify operating points that balance fidelity and utility rather than forcing a single-loss compromise.

Based on the present findings, we recommend that future EEG denoising studies include a minimal downstream evaluation protocol: (i) report matched denoised/denoised classification accuracy on at least one established BCI or clinical paradigm alongside reconstruction metrics; (ii) include both a linear spatial-filter decoder (e.g., CSP+LDA) and at least one end-to-end neural decoder to expose classifier-dependent effects; and (iii) test on naturally recorded trials without synthetic artifact injection to confirm that denoiser effects generalize beyond the semi-synthetic training distribution.

5.4 Limitations

This study characterizes the capacity requirements and downstream utility of the dominant supervised EEG denoising evaluation paradigm; it does not claim that all real-world denoising tasks are equally low-dimensional. The capacity sweep was conducted on single-channel inputs, consistent with the EEGDenoiseNet benchmark protocol that serves as the primary evaluation standard in the field. A focused 22-channel multichannel denoiser control confirmed that the CSP+LDA downstream gap is not an artifact of independent per-channel processing (Table 8), but multichannel reconstruction benchmarking and deployment-optimized multichannel architectures are beyond the scope of this study.

The primary reconstruction benchmarks are semi-synthetic, which is the standard evaluation paradigm for supervised EEG denoising. To test whether conclusions transfer beyond semi-synthetic conditions, we evaluated denoisers on naturally recorded BCI IV-2a trials without synthetic artifact injection (Table 7); the CSP+LDA utility gap persisted. Downstream evaluation focused on motor imagery across all nine BCI IV-2a subjects and five decoder families rather than spanning multiple BCI paradigms or clinical tasks. This within-paradigm depth with nine subjects, five classifiers, three artifact types, and real and synthetic conditions prioritizes statistical rigor over paradigm breadth.

The controlled same-pipeline baseline comparisons cover EEGDN CNN, MicroWaveNet, and a Patch-Transformer capacity sweep as a second-family control. CT-DCENet could not be independently verified because the official code was unavailable; its literature-reported values are retained as uncontrolled reference points and labeled as such. The Patch-Transformer control confirms that the diminishing-return pattern is not specific to depthwise-separable U-Nets, and the convergence of both families toward the same saturation pattern supports generality beyond a single architecture template.

6 Conclusion

Standard EEG denoising benchmarks saturate with compact models: 3–6.5K parameters recover most reconstruction performance, and the pattern holds across the primary DSConv family, controlled baseline retraining, and a second-family Patch-Transformer control. Same-pipeline evidence shows that benchmark difficulty is far below the million-parameter regime, and that the marginal reconstruction gains reported by larger models come at parameter costs of 200–1000× with no demonstrated downstream benefit.

Reconstruction-optimized denoising degrades spatial-filter motor-imagery classification across artifact types and on real non-synthetic recordings, while end-to-end neural decoders show variable effects. Reconstruction fidelity is therefore necessary but not sufficient for judging EEG denoising utility.

For edge EEG, base4–base6 models at 33–46 KB are the recommended operating points from this study. EEG denoising should be evaluated not only by fidelity to a reconstructed reference, but by whether it preserves the neural information that downstream applications require. We recommend that denoising papers report matched classifier accuracy on at least one BCI or clinical paradigm, using both linear and end-to-end decoders, to detect the classifier-dependent utility effects that reconstruction metrics alone cannot capture.

Author Contributions

J.S.B. conceived the idea, designed the experiments, and implemented them. S.R.C. and S.P. supervised the research. All authors reviewed and approved the final manuscript.

Conflicts of Interest

The authors declare no conflicts of interest.

Funding

This research received no specific grant from any funding agency in the public, commercial, or not-for-profit sectors.

Data availability

The EEGDenoiseNet benchmark dataset is publicly available [1]. BCI Competition IV datasets are available from the competition website. The Mixed-1M corpus generation code, model training code, evaluation scripts, and checkpoint generation will be made available upon publication of the peer-reviewed version of this work.

Ethical Statement

This study used exclusively publicly available benchmark datasets (EEGDenoiseNet and BCI Competition IV). These datasets were collected and published under ethical approvals obtained in the original studies. No new human or animal data were collected for this work.

References

References

- [1] Zhang H, Zhao M, Wei C, Mantini D, Li Z and Liu Q 2021 *Journal of Neural Engineering* **18** 056057
- [2] Chuang C H, Chang K Y, Huang C S and Jung T P 2022 *NeuroImage* **263** 119586
- [3] Dong Y, Tang X, Li Q, Wang Y, Jiang N, Tian L, Zheng Y, Li X, Zhao S, Li G and Fang P 2023 *IEEE Transactions on Neural Systems and Rehabilitation Engineering* **31** 3524–3534
- [4] Tang Y, Huang W, Chen C and Chen D 2025 *IEEE Journal of Biomedical and Health Informatics* **29** 4095–4108
- [5] Chen W, Li Y, Zheng N and Shi W 2025 *IEEE Journal of Biomedical and Health Informatics* **29** 6551–6564
- [6] Croft R J and Barry R J 2000 *Neurophysiologie Clinique/Clinical Neurophysiology* **30** 5–19
- [7] Urigüen J A and Garcia-Zapirain B 2015 *Journal of Neural Engineering* **12** 031001
- [8] Gratton G, Coles M G H and Donchin E 1983 *Electroencephalography and Clinical Neurophysiology* **55** 468–484
- [9] Makeig S, Bell A J, Jung T P and Sejnowski T J 1996 Independent component analysis of electroencephalographic data *Advances in Neural Information Processing Systems* vol 8 pp 145–151
- [10] Jung T P, Makeig S, Humphries C, Lee T W, McKeown M J, Iragui V and Sejnowski T J 2000 *Psychophysiology* **37** 163–178

- [11] Mullen T R, Kothe C A E, Chi Y M, Ojeda A, Kerth T, Makeig S, Jung T P and Cauwenberghs G 2015 *IEEE Transactions on Biomedical Engineering* **62** 2553–2567
- [12] Chang C Y, Hsu S H, Pion-Tonachini L and Jung T P 2020 *IEEE Transactions on Biomedical Engineering* **67** 1114–1121
- [13] Nolan H, Whelan R and Reilly R B 2010 *Journal of Neuroscience Methods* **192** 152–162
- [14] Mognon A, Jovicich J, Bruzzone L and Buiatti M 2011 *Psychophysiology* **48** 229–240
- [15] Roy Y, Banville H, Albuquerque I, Gramfort A, Falk T H and Faubert J 2019 *Journal of Neural Engineering* **16** 051001
- [16] Yue X, Lu L, Liu H and Zang Y 2025 *CNS Neuroscience & Therapeutics* **31** e70632
- [17] Gao T, Chen D, Tang Y, Ming Z and Li X 2023 *IEEE Journal of Biomedical and Health Informatics* **27** 1283–1294
- [18] Yin J, Liu A, Li C, Qian R and Chen X 2025 *IEEE Journal of Biomedical and Health Informatics* **29** 3930–3941
- [19] Chen J, Pi D, Jiang X, Xu Y, Chen Y and Wang X 2024 *IEEE Transactions on Instrumentation and Measurement* **73** 1–16
- [20] Yu J, Li C, Lou K, Wei C and Liu Q 2022 *Journal of Neural Engineering* **19** 026052
- [21] Lahiri J B, Kulkarni A and Panwar S 2025 MicroWaveNet: Lightweight CBAM-augmented wavelet-attentive networks for robust EEG denoising *2025 IEEE 35th International Workshop on Machine Learning for Signal Processing (MLSP)* pp 1–6
- [22] Huang J, Wang C, Zhao W, Grau A, Xue X and Zhang F 2024 *IEEE Transactions on Consumer Electronics* **70** 5561–5575
- [23] Lawhern V J, Solon A J, Waytowich N R, Gordon S M, Hung C P and Lance B J 2018 *Journal of Neural Engineering* **15** 056013
- [24] Chollet F 2017 Xception: Deep learning with depthwise separable convolutions *Proceedings of the IEEE Conference on Computer Vision and Pattern Recognition* pp 1251–1258
- [25] Howard A G, Zhu M, Chen B, Kalenichenko D, Wang W, Weyand T, Andreetto M and Adam H 2017 *arXiv preprint arXiv:1704.04861 (Preprint 1704.04861)*
- [26] Wang Q, Wu B, Zhu P, Li P, Zuo W and Hu Q 2020 ECA-Net: Efficient channel attention for deep convolutional neural networks *Proceedings of the IEEE/CVF Conference on Computer Vision and Pattern Recognition* pp 11531–11539
- [27] Han S, Mao H and Dally W J 2016 Deep compression: Compressing deep neural networks with pruning, trained quantization and huffman coding *International Conference on Learning Representations*
- [28] Bigdely-Shamlo N, Mullen T, Kothe C, Su K M and Robbins K A 2015 *Frontiers in Neuroinformatics* **9** 16
- [29] Nagar S, Kumar A and Swamy M N S 2021 *Signal Processing* **188** 108225
- [30] Kaplan J, McCandlish S, Henighan T, Brown T B, Chess B, Child R, Gray S, Radford A, Wu J and Amodei D 2020 *arXiv preprint arXiv:2001.08361 (Preprint 2001.08361)*
- [31] Frankle J and Carbin M 2019 The lottery ticket hypothesis: Finding sparse, trainable neural networks *International Conference on Learning Representations*
- [32] Delorme A and Makeig S 2004 *Journal of Neuroscience Methods* **134** 9–21
- [33] Obeid I and Picone J 2016 *Frontiers in Neuroscience* **10** 196
- [34] Tangermann M, Müller K R, Aertsen A, Birbaumer N, Braun C, Brunner C, Leeb R, Mehring C, Miller K J, Müller-Putz G R, Nolte G, Pfurtscheller G, Preissl H, Schalk G, Schlögl A, Vidaurre C, Waldert S and Blankertz B 2012 *Frontiers in Neuroscience* **6** 55

- [35] Charbonnier P, Blanc-Féraud L, Aubert G and Barlaud M 1994 Two deterministic half-quadratic regularization algorithms for computed imaging *Proceedings of the IEEE International Conference on Image Processing* vol 2 pp 168–172
- [36] Pfurtscheller G and Neuper C 2001 *Proceedings of the IEEE* **89** 1123–1134
- [37] Ramoser H, Müller-Gerking J and Pfurtscheller G 2000 *IEEE Transactions on Rehabilitation Engineering* **8** 441–446
- [38] Blankertz B, Tomioka R, Lemm S, Kawanabe M and Müller K R 2008 *IEEE Signal Processing Magazine* **25** 41–56
- [39] Lotte F, Bougrain L, Cichocki A, Clerc M, Congedo M, Rakotomamonjy A and Yger F 2018 *Journal of Neural Engineering* **15** 031005
- [40] Parra L C, Spence C D, Gerson A D and Sajda P 2005 *NeuroImage* **28** 326–341
- [41] Haufe S, Meinecke F, Görgen K, Dähne S, Haynes J D, Blankertz B and Bießmann F 2014 *NeuroImage* **87** 96–110
- [42] Schirrneister R T, Springenberg J T, Fiederer L D J, Glasstetter M, Eggenesperger K, Tangermann M, Hutter F, Burgard W and Ball T 2017 *Human Brain Mapping* **38** 5391–5420
- [43] Song Y, Zheng Q, Liu B and Gao X 2023 *IEEE Transactions on Neural Systems and Rehabilitation Engineering* **31** 710–719
- [44] Xiang T Y, Lei Z, Zhou X H, Xie X L, Liu S Q, Gui M J, Ou H Y, Huang X Z, Fu X Y and Hou Z G 2025 Task-oriented learning for automatic EEG denoising (*Preprint* [2509.14665](#))